Efficient and accurate FDTD algorithm for the treatment of curved material boundaries

H. Yang
C.J. Railton

Indexing terms: FDTD methods, Curved boundaries, Electromagnetic structures

Abstract: The application of finite-difference time-domain methods to the analysis of structures having curved boundaries is a long-standing problem. Traditionally, either the staircasing approximation which is simple but inaccurate, or the generalised nonorthogonal grids which are accurate but complex have been used. In this contribution a novel approach is presented which combines the efficiency of the Cartesian mesh with the accuracy of the conformal grid. Results are presented for some example structures which are in good agreement with other methods.

1 Introduction

Finite-difference time-domain (FDTD) methods originally put forward by Yee [1] have proved to be very efficient numerical algorithms in computational electromagnetics. However, the traditional FDTD algorithm is based on a Cartesian co-ordinate system, and it is difficult to generate meshes exactly for electromagnetic structures with curved boundaries. It is usual to utilise a staircase approximation in the FDTD method for curved structures and an accurate solution can only be obtained by using very fine grids and consequently, a very small time step. In addition, the staircase approximation of the physical boundary of a resonator will often result in a failure to detect all the resonant modes and in the prediction of Q factors which are lower than in reality. Apart from the staircase approximation, there are two main modifications to the FDTD method which have been put forward to analyse the electromagnetic structures with curved boundaries: the contour path (CPFDTD) algorithm [2–5], and the nonorthogonal FDTD method [6–9]. The CPFDTD algorithm is based on the integral form of Ampere's and Faraday's laws. The update equations must be modified in those distorted cells which are near the curved boundaries. This is readily achieved for curved perfect conductors because the tangential components of the electric field on the boundaries are zero. Even so, although good results have been obtained by Jurgens, [2, 3], the generation of the mesh is nontrivial and, in addition, it has been shown that the basic scheme must be modified to ensure stability [4, 5]. For dielectric objects, where the tangential E field is nonzero, additional equations are needed to calculate the tangential components of electric field from the equation of Ampere's law. This makes the algorithm much more complex and unwieldy and, with the exception of a simple 2D example in [2], no published results are known to the authors.

The generalised nonorthogonal FDTD algorithm was put forward by Holland [6] and refined by others [7, 8]. The underlying mathematics dealing with the geometry and its application to electromagnetic fields can be found in [10]. Many numerical results have been obtained successfully [7, 8, 11]. However, compared with the conventional FDTD scheme, two additional equations are needed in each iteration step to realise the transform between the contravariant and covariant components of electric and magnetic fields. Moreover, extra computer memory is needed to store the metric tensor of both E and H nodes, which are essential parameters in nonorthogonal co-ordinate systems. For these reasons, the method is limited to relatively small structures. Although the nonorthogonal FDTD scheme is a generalised method, it is difficult to make it compatible with existing FDTD software which is based on the Cartesian co-ordinate system.

To take advantage of the nonorthogonal FDTD algorithm which is powerful for the computation of structures with curved boundaries, we have developed a combined method, which uses the theory of the nonorthogonal FDTD scheme within an underlying Cartesian co-ordinate system. In the combined method most of the grid is in the Cartesian co-ordinate system with only those cells near the curved boundaries being treated as nonorthogonal cells. The relative advantages and disadvantages of the new method compared with existing techniques are given in Table 1.

Table 1: Advantages (+) and disadvantages (–) of methods

	CPFDTD	Nonorthogonal	This research
Computer resources	+	–	+
Accuracy	–	+	+
General material boundaries	–	+	+
Ease of mesh generation	+	–	+

IEE Proceedings online no. 19971226

Paper first received 29th November 1996 and in revised form 28th February 1997

The authors are with the Centre for Communications Research, Faculty of Engineering, University of Bristol, Bristol BS8 1UB, UK

The fundamental concepts and some simulation work using the combined method on closed curved metal structures have been presented in [12]. In this contribution the method is developed to allow the electromagnetic analysis of dielectrically loaded waveguides with arbitrary cross-sections, which include dielectric rod and slabs inside rectangular and circular waveguides. The simulation results will be compared with those from analytical method and the FDTD methods using the staircase approximation.

2 Description of new method

The new FDTD algorithm which combines the advantages of the nonorthogonal FDTD program with conventional Cartesian FDTD technique has been used to compute the cut-off frequencies of circular, rectangular and elliptical hollow waveguides. In the combined algorithm, the majority of the mesh is Cartesian which allows the use of the conventional FDTD and only near the oblique surfaces are non-Cartesian cells used. This leads to a more accurate formulation than CPFDTD but much less computational resources than a generalised nonorthogonal method.

A good understanding of the algorithm can be started by considering the metric tensor, which is one of the important components in the analysis of vectors in a nonorthogonal co-ordinate system. It can be obtained from $g_{ij} = \vec{A}_i \cdot \vec{A}_j$, where $\vec{A}_i$, $\vec{A}_j$ are the bases of a covariant vector. For an orthogonal co-ordinate system only the diagonal components will be nonzero (as shown in eqn. 1). Moreover, the contravariant and covariant components will be collinear in an orthogonal co-ordinate system. Extra memory is not needed to store the metric tensors and contravariant or covariant components. Only the values of those parts of the mesh which are close to the material boundaries need to be stored.

$$\begin{aligned} g_{ij} &= \vec{A}_i \bullet \vec{A}_j = |a_i a_j| \cdot \cos\theta_{ij} \\ &= |a_i a_j| \cdot \delta_{ij} \quad \text{if } \vec{A}_i, \vec{A}_j \text{ are orthogonal} \\ \delta_{ij} &= \begin{cases} 1 & i = j \\ 0 & i \neq j \end{cases} \end{aligned} \tag{1}$$

θ_{ij} is the angle between two generalised axes, which it is easy to obtain when these axes are straight lines, otherwise, the angle can be obtained from their tangential lines.

2.1 Generation of the meshes

Let an arbitrary curve pass through a standard FDTD cell so that the original cell is bisected. The two basic types of cells near the curved boundary are defined as either 'flag' or 'triangle'. In 'flag' cells the original cell is split by the material boundary into two cells which are still quadrilateral. In this case the neighbouring cell is extended as shown in Fig. 1 and the E_x or E_z node is replaced by an E_t node on the material boundary. The second type of cell, called a 'triangle', can not be treated directly as an FDTD cell, the mesh needs to be reconstructed so that all the cells are quadrilateral. To do this, an additional point is defined on the material boundary, such as C' in Fig. 2 and the edges of the intercepted cell and its neighbours are modified as also shown in Fig. 2. The new nonorthogonal FDTD meshes on the curved boundary for those triangular and quadrilateral meshes are then obtained. It is not difficult to establish the functions of the two types of cells. The 'triangle' cell is always placed where the curvature of a curved boundary changes abruptly. To some extent, it looks like the triangular element near the curved boundary in the finite-element method. The difference is that in FDTD the 'triangle' is actually a generalised quadrilateral cell, and the vector of the electromagnetic field is denoted in a nonorthogonal co-ordinate system. The 'flag' cells always appear on the curved boundary while the curvature changes slowly. In general, these two cells are enough to denote a curved or an oblique boundary in FDTD computations in the underlying Cartesian co-ordinate system.

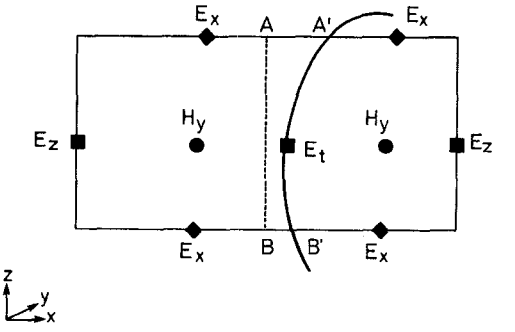

Fig. 1 *'Flag' cell extending to neighbouring cells*

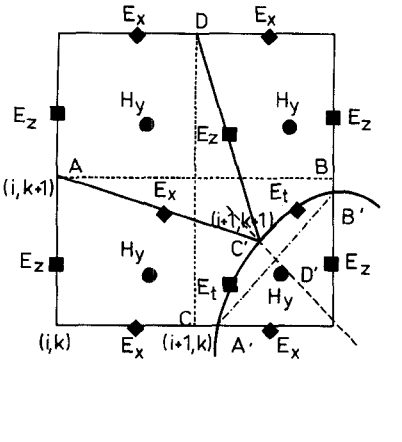

Fig. 2 *Reconstruction of a 'triangle' cell*

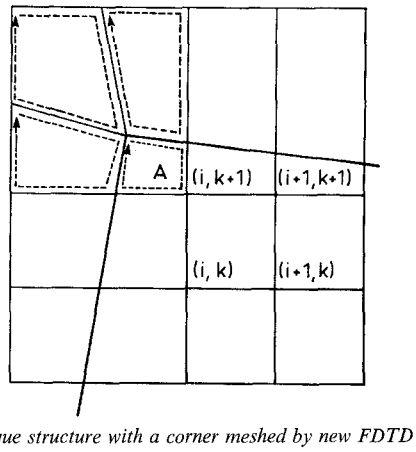

Fig. 3 *Oblique structure with a corner meshed by new FDTD method*

2.2 Treatment of corners in angular objects

If we consider oblique structures with corners, such as the rotated rectangular waveguide shown as Fig. 3, the cell containing the corner will be treated as a 'triangle', but in this case the extra node point is placed precisely on the corner. By this means, the exact position of the

corners has been taken into consideration, leading to improved accuracy. The example of an oblique rectangular disk modelled by CPFDTD is shown in Fig. 4. It shows that the small quadrilateral area labelled A has not been taken into consideration in the CPFDTD mesh. This will introduce an inaccuracy if the mesh is coarse, which is avoided in the method described here.

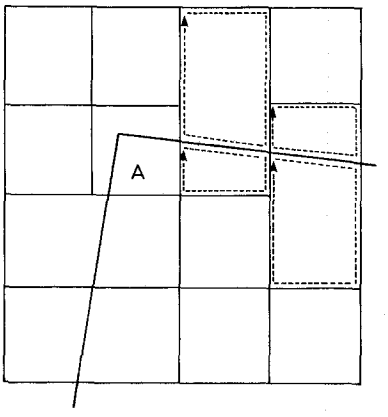

Fig. 4 *Oblique structure with a corner meshed by CPFDTD*

2.3 Choosing the position of the nodes in modified cells

Once the new co-ordinates including those 'triangle' and 'flag' cells are determined, it is easy to set the E and H nodes in each cell. Following Yee's scheme, the middle points of the cell boundaries are chosen on the x axis and the z axis, respectively, as E_x and the centroid of the cell as H nodes, but x, y, z cannot now be regarded as Cartesian co-ordinates. This arrangement of field nodes allows existing FDTD algorithms which have been developed for a Cartesian co-ordinate system to be immediately incorporated into new FDTD program. These include absorbing boundary conditions and near-far field transformations. A further advantage of the new FDTD scheme is that it reduces to conventional FDTD codes when those structures to be studied are simple rectangles. Those components of electric field (for TE modes) and magnetic field (for TM modes) on the interface of material are moved along the boundary, which is used to approximate the curvature of structures in practical computer programming. Having determined the node position is of the electric and magnetic fields, the components of the metric tensor g_{ij} in nonorthogonal cells can be calculated and stored (shown as eqn. 1).

3 FDTD iteration formulae in new meshes

In the previous Section, the meshing of a curved boundary on a Cartesian co-ordinate system was defined. This approach ensures that the new mesh conforms both to the material boundaries and to the surrounding Cartesian mesh. Thus the conventional FDTD approach can be used on the Cartesian cells and nonorthogonal method on the nonorthogonal cells, and the values are passed directly to the common nodes without the need for interpolation.

As an example, consider the structure shown in Fig. 3. Cell (i, k) is a Cartesian node and the traditional FDTD iteration formula shown in eqn. 2 can be used to obtain the E and H components. During iteration, the covariant and contravariant components need not be introduced, and therefore the memory requirements are the same as for the standard FDTD

$$
\begin{aligned}
&E_x^{n+1}(i,k) \\
&= E_x^n(i,k) - \frac{\delta t}{c\varepsilon_r \delta z}[H_y^{n+\frac{1}{2}}(i,k) - H_y^{n+\frac{1}{2}}(i,k-1)] \\
&E_z^{n+1}(i,k) \\
&= E_z^n(i,k) + \frac{\delta t}{c\varepsilon_r \delta x}[H_y^{n+\frac{1}{2}}(i,k) - H_y^{n+\frac{1}{2}}(i-1,k)] \\
&H_y^{n+\frac{1}{2}}(i,k) \\
&= H_y^{n-\frac{1}{2}}(i,k) + \frac{\delta t}{c\mu_r \delta x}[E_z^n(i+1,k) - E_z^n(i,k)] \\
&\quad - \frac{1}{\mu_r \delta z}[E_x^n(i,k+1) - E_x^n(i,k)] \qquad (2)
\end{aligned}
$$

where δx and δz are variable space steps given by

$$\delta x = |x_{i+1} - x_i|$$
$$\delta z = |z_{j+1} - z_j|$$

The contravariant and covariant components of the E and H fields on the nonorthogonal cells can be defined as

$$E_i = \vec{E} \cdot \vec{A}_i \qquad H_i = \vec{H} \cdot \vec{A}_i$$
$$E^j = \vec{E} \cdot \vec{A}^j \qquad H^j = \vec{H} \cdot \vec{A}^j$$
$$i, j = x, y \text{ or } z$$

where the covariant vector bases of the vector $\mathbf{A}(\mathbf{A}_x$ and $\mathbf{A}_z)$ are defined along the x and z axes, respectively, and their dual bases, known as the contravariant bases ($\mathbf{A}^x$ and $\mathbf{A}^z$), are defined to be orthogonal to the original bases $\mathbf{A}_z$ and $\mathbf{A}_x$, which are shown in Fig. 5 (2D cases only).

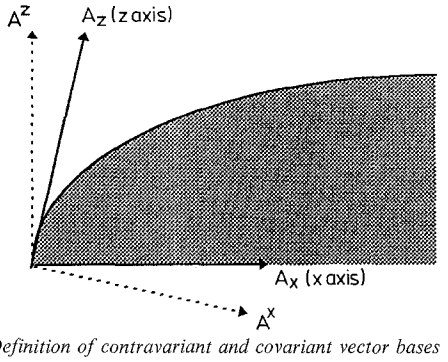

Fig. 5 *Definition of contravariant and covariant vector bases*

Cell (i + 1, k + 1) is a nonorthogonal node, so the nonorthogonal FDTD method is used to find the values of the E and H components. The equations for this cell are shown as

$$
\begin{aligned}
&E^x(i+1,k+1)^{n+1} \\
&= E^x(i+1,k+1)^n \\
&\quad + \frac{\delta t}{c\varepsilon_r}[H_y(i+1,k) - H_y(i+1,k+1)]^{n+\frac{1}{2}} \\
&\quad \cdot \sqrt{\frac{1}{g_{yy}}} \cdot \sqrt{\frac{g_{xx}}{g}} \\
&E^z(i+1,k+1)^{n+1} \\
&= E^z(i+1,k+1)^n \\
&\quad + \frac{\delta t}{c\varepsilon_r}[-H_y(i,k+1) + H_y(i+1,k+1)]^{n+\frac{1}{2}} \\
&\quad \cdot \sqrt{\frac{1}{g_{yy}}} \cdot \sqrt{\frac{g_{zz}}{g}}
\end{aligned}
$$

$$H^y(i+1,k+1)^{n+\frac{1}{2}}$$
$$= H^y(i+1,k+1)^{n+\frac{1}{2}} + \frac{\delta t}{c\mu_r}\cdot\sqrt{\frac{g_{yy}}{g}}$$
$$\cdot\left[\frac{E_z(i+2,k+1)}{\sqrt{g_{zz}(i+2,k+1)}} - \frac{E_z(i+1,k+1)}{\sqrt{g_{zz}(i+1,k+1)}}\right.$$
$$\left. - \frac{E_x(i+1,k+2)}{\sqrt{g_{xx}(i+1,k+2)}} + \frac{E_x(i+1,k+1)}{\sqrt{g_{xx}(i+1,k+1)}}\right]^{n-\frac{1}{2}} \quad (3)$$

In the above equations, the contravariant components in cell (i, k) need not be transformed into covariant components because they are collinear in Cartesian cells. In nonorthogonal cells, transformation is necessary, using eqn. 4.

$$E_x(i+1,k+1) = G_{xx}E^x(i+1,k+1)$$
$$+\frac{G_{xz}}{4}\left[E^z\left(i+1+\frac{1}{2},k+1-\frac{1}{2}\right)\right.$$
$$+E^z\left(i+1-\frac{1}{2},k+1-\frac{1}{2}\right)$$
$$+E^z\left(i+1+\frac{1}{2},k+1+\frac{1}{2}\right)$$
$$\left.+E^z\left(i+1-\frac{1}{2},k+1+\frac{1}{2}\right)\right]$$
$$H_y(i+1,k+1) = H^y(i+1,k+1)$$
$$G_{xz} = \sqrt{\frac{g_{xx}}{g_{zz}}}\cdot g_{xz} \quad (4)$$

where x, y, z denote generalised co-ordinates in a nonorthogonal co-ordinate system, they will reduce to Cartesian co-ordinates in those Cartesian cells.

For the conventional FDTD algorithm, the boundary condition of the material interfaces has automatically been taken into consideration in eqns. 3 and 4. In this paper all outer boundaries of waveguides are assumed to be perfect metal, so one can let $\varepsilon \to \infty$ in the formulae. For dielectric materials, one simply inputs the value of permittivity, and allows $\varepsilon = 1$ if it is in a free space. It should be emphasised here that all the above equations can be rewritten so as to include materials of finite conductivity. In this case the methods used in conventional FDTD can be directly applied to the new algorithm.

4 Numerical results

Several numerical examples of useful dielectric-loaded waveguides are presented in this Section. The structures considered here are: first, dielectric-slab-loaded waveguides with homogeneous and inhomogeneous fillings; secondly, dielectric-rod-loaded square waveguides; and finally, circular waveguides loaded with dielectric cylinders. The numerical results obtained using the new FDTD algorithm will be compared with data from other methods such as the variation-iteration method [13], analytical method [14], [15] and FDTD method by staircase approximation.

4.1 Dielectric-slab-loaded waveguides with homogeneous or inhomogeneous fillings

Fig. 6 shows the mesh of the slab-dielectric-loaded waveguide, where all the cells which are near to the material boundary have been made conformal to the material. The position of the slab in the rectangular shield with the dimensions $b/a = 0.5$, $a = 0.3$m can be described as $x_1 = (a - t)/2$, $x_2 = (a + t)/2$, where a and b are the width and height of the rectangular waveguide, respectively, and t is the thickness of the dielectric slab. As presented in the previous Section, this combined method shows the advantage of dealing with electromagnetic structures with corners which do not coincide with the Cartesian mesh boundary. This avoids the constraints involved in choosing the grid sizes in the standard or graded grid FDTD algorithm which result from ensuring that the mesh coincides with the material boundaries. Fig. 7 shows the results for the cut-off frequencies of the LSE_{10} mode as functions of t and ε_r of the homogeneous dielectric slab.

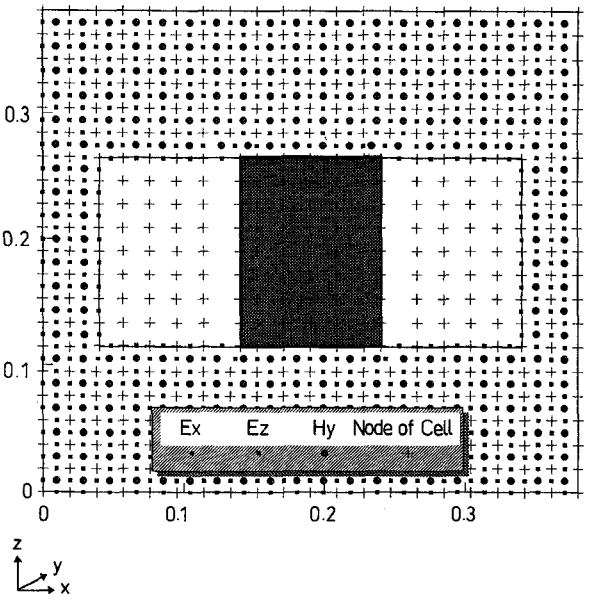

Fig. 6 *Dielectric-slab-loaded waveguide meshed in Cartesian grids*

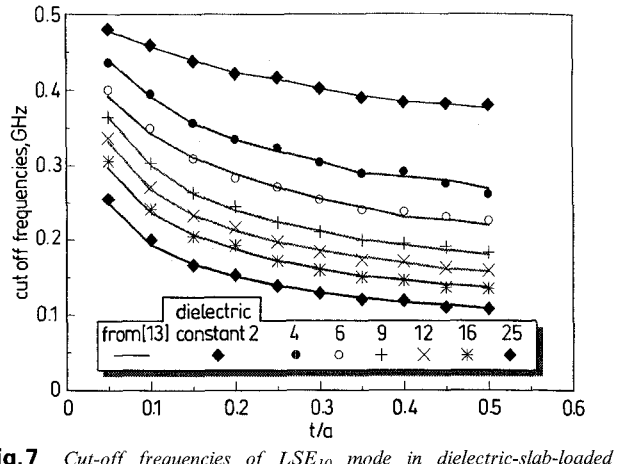

Fig. 7 *Cut-off frequencies of LSE_{10} mode in dielectric-slab-loaded waveguides*

They show a good agreement with the results by Yu and Chu [13]. In this case, the dielectric-loaded waveguide is meshed by 14 × 14 cells with the computation area of 0.38m × 0.38m. Table 2 shows the cut-off frequencies of some higher order modes existing in the homogeneous dielectric-slab-loaded waveguide with $\varepsilon_r = 2$. Results by FDTD algorithm with staircase approximation are also listed in Table 2. The approximate algorithm fails to detect all of the resonant modes and shows less accuracy than the combined FDTD.

Table 2: Results of cut-off frequencies (GHz) of LSE_{mn} modes in a homogeneous dielectric centrally loaded waveguide with $b/a = t/a = 1/2$, $x_1 = (a - t)/2$, $x_2 = (a + t)/2$, and $\varepsilon_r(x) = 2$

Modes	Combined FDTD (14 × 14)	Combined FDTD (28 × 28)	Staircase FDTD (14 × 14)	Staircase FDTD (28 × 28)	Staircase FDTD (50 × 50)	From [13]
LSE_{10}	0.3718	0.3718	—	—	—	0.3701
LSE_{20}	0.7984	0.8080	0.7348	0.7855	0.7940	0.8058
LSE_{11}	0.8151	0.8240	—	—	—	0.8224
LSE_{21}	1.1846	1.1883	1.0929	—	—	1.1261
LSE_{30}	1.2346	1.2608	1.1144	—	—	1.2739
LSE_{12}	1.4634	1.5039	1.3562	1.3898	1.4981	1.4970
LSE_{31}	1.6183	1.5397	1.4939	—	—	1.5244
LSE_{40}	1.7018	1.6636	1.5835	1.6615	1.6674	1.6978
LSE_{22}	1.8066	1.7542	1.6771	—	—	1.7331
LSE_{41}	1.8948	1.9091	1.7890	1.8283	—	1.9083

It is interesting to note that in some cases the use of a finer staircased mesh leads to more modes being missed. The corresponding results in the offset dielectric-loaded waveguide are listed in Table 3. Both of them show a good agreement with values given by [13].

Table 3: Results of cut-off frequencies (GHz) of LSE_{mn} modes in a homogeneous dielectric offset loaded waveguide with $b/a = t/a = 1/2$, $x_1 = t$, $x_2 = a$, and $\varepsilon_r(x) = 2$

Modes	From combined FDTD (28 × 28)	From [13]
LSE_{10}	0.3980	0.4029
LSE_{20}	0.8413	0.8489
LSE_{11}	0.8699	0.8666
LSE_{21}	1.2012	1.2151
LSE_{30}	1.2251	1.2195
LSE_{31}	1.4396	1.4837
LSE_{12}	1.4849	1.5291
LSE_{40}	1.6755	1.6750
LSE_{22}	1.8185	1.8315
LSE_{41}	1.8972	1.8691

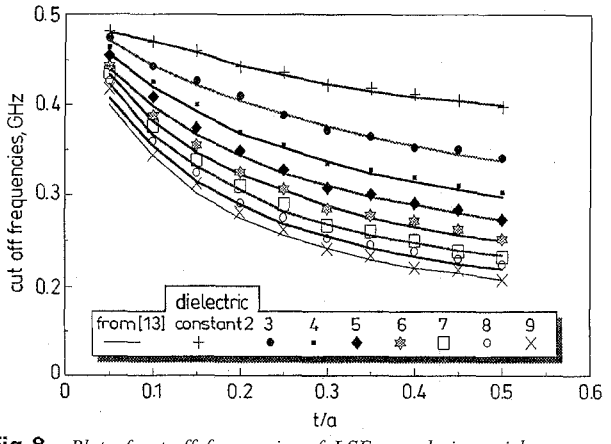

Fig.8 *Plot of cut-off frequencies of LSE_{10} mode in an inhomogenous dielectric-slab-loaded waveguide*

Calculations were also carried out for the case of an inhomogeneous dielectric filling with $\varepsilon_r = 4(\varepsilon_{r,\max} - 1)(x - x_1)(x_2 - x)/(x_2 - x_1)$. The cut-off frequencies of the waveguide of LSE_{10} mode with various slab thickness and different dielectric $\varepsilon_{r,\max}$ values were calculated. In the simulation, it is difficult to obtain more precise results for those thinner slabs in the waveguide, as many more sampling points are needed to describe the variations of the inhomogeneous dielectric material. The results for the cut-off frequencies showing an average error of approximately 1.5% for a 14 × 14 mesh and 0.5% for a 28 × 28 mesh on waveguides with inhomogeneous dielectric fillings are presented in Figs. 8 and 9.

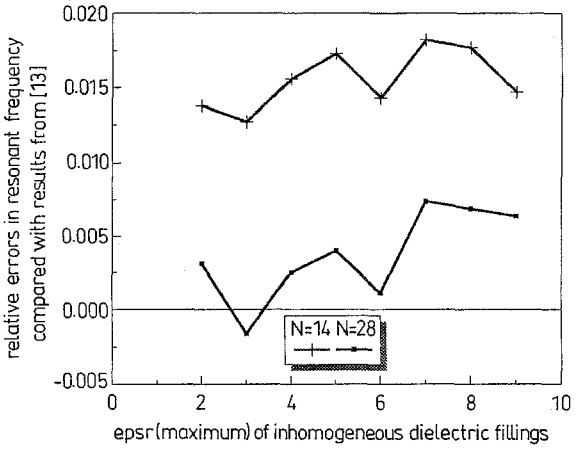

Fig.9 *Errors achieved by different meshes*

4.2 Dielectric-rod-loaded square waveguides

A square waveguide (side length A) with a centred dielectric rod (radius a_0) will be investigated in this section. This exemplifies the meshing of a dielectric-loaded electromagnetic structure with curved boundaries within a Cartesian mesh. The mesh is shown in Fig. 10, which indicates that the computational region of 0.38m × 0.38m is meshed by 14 × 14 cells. The modes in this structure are very complicated and their properties have been studied in [14]. The simulation results using the combined FDTD method are displayed in Fig. 11 where they compared with values from [14] and also show good agreement with them. All expected higher-order modes are detected. The displayed results show the cut-off frequencies of HE modes in the guides plotted against rod radius and confirm the validity of the combined FDTD algorithm.

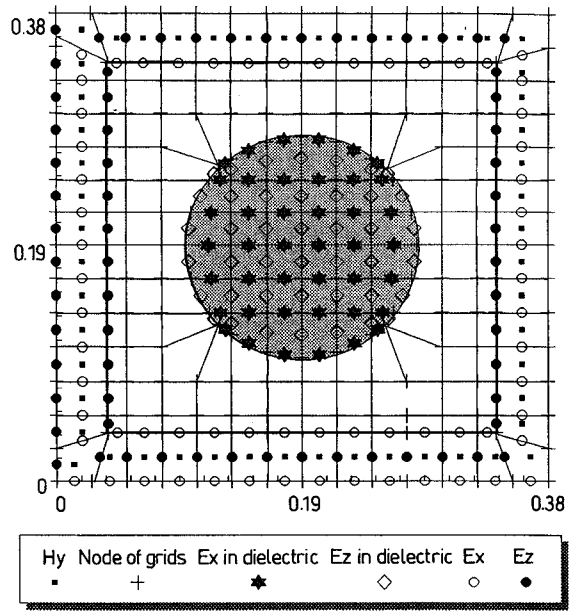

Fig. 10 *Dielectric-rod-loaded square waveguide structure meshed in Cartesian grids*

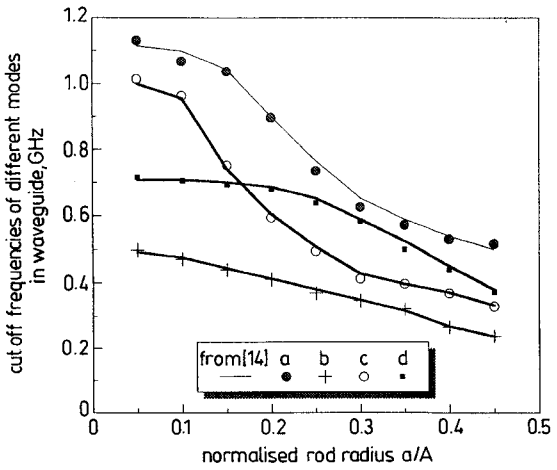

Fig. 11 *Cut-off frequencies of different modes in the dielectric-rod-loaded square waveguide*
a: HE_{21}^{eo}, HE_{12}^{eo}; *b*: HE_{10}^{eo}, HE_{21}^{01}; *c*: HE_{20}^{00}, HE_{02}^{00}; *d*: HE_{11}^{ee}

4.3 Circular waveguides with dielectric cylinders

Fig. 12 shows the structure of a uniform circular guide consisting of two concentric dielectric cylinders. The radius of the inner one is a with a relative permittivity ε_1, and the radius of the outer one is b with a relative permittivity ε_2. The dominant modes in it are angularly symmetric E_{0n} or H_{0n} modes [15]. To determine the cut-off frequencies it is possible to solve the transcendental equations which contain radial functions. This is a complicated process compared with numerical methods. Table 4 gives the cut-off frequencies of the dominant TM mode in the waveguide calculated using the combined algorithm and the staircase approximation of the FDTD method using two different cell sizes. This shows that with the staircase approximation, the solutions only converge when a fine mesh is used whereas, with the combined method accurate results are obtained using only 12 × 12 mesh.

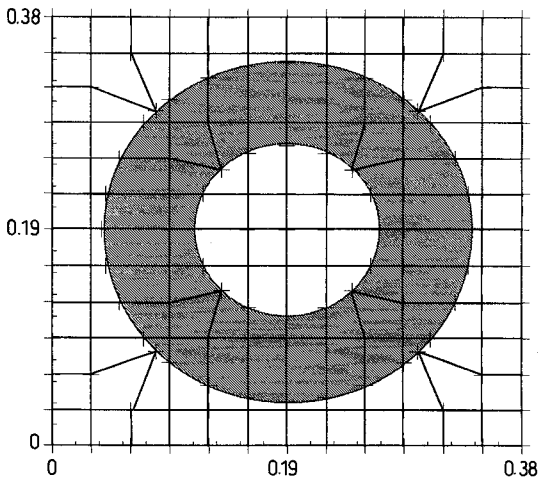

Fig. 12 *Circular guide with dielectric cylinders meshed in Cartesian grids*

5 Conclusion

A new FDTD scheme has been introduced, which is based on using a nonorthogonal FDTD algorithm so as to deal with an arbitrary electromagnetic structure on an underlying Cartesian grid. The validity has been confirmed by the simulation of dielectrically-loaded waveguides with arbitrary cross-sections. The new combined method has the benefit of reduced computer resources and easily generated meshes when compared with schemes based on generalised nonorthogonal coordinate systems and of improved accuracy when compared to a staircase approximation. The numerical simulation shows that the new method is very efficient and the results are in excellent agreement with those from other methods. The application and extension of the method to three dimensional structures is being studied and will be reported in a future contribution.

6 Acknowledgment

The authors wish to thank the Committee of Vice-Chancellors and Principals (UK) for the provision of

Table 4: Cut-off frequencies (GHz) of the lowest E mode in circular guide with dielectric cylinders (b/a = 2, ε_1 = 1)

ε_2	Combined FDTD (12 × 12)	Combined FDTD (14 × 14)	FDTD staircase approximation (12 × 12)	FDTD staircase approximation (72 × 72)
2.54	0.5822	0.5912	0.5510	0.5938
10.2	0.3195	0.3231	0.3027	0.3357
23.0	0.2145	0.2196	0.2050	0.2247
53.0	0.1430	0.1447	0.1360	0.1491
96.0	0.1073	0.1070	0.1012	0.1069

an ORS award during Mr Hao's PhD study and also thank Professor Joe McGeehan for the provision of facilities at the Centre for Communications Research. They also wish to thank Dr Ian Craddock and Dr Ma Lizhuang for some useful discussion.

7 References

1 YEE, K.S.: 'Numerical solution of initial boundary value problems involving Maxwell's equations in isotropic media', *IEEE Trans.*, 1966, **AP-14**, pp. 302–307
2 JURGENS, T.G., TAFLOVE, A., UMASHANKAR, K., and MOORE, T.G.: 'Finite-difference time-domain modelling of curved surfaces', *IEEE Trans.*, 1992, **AP-40**, pp. 357–366
3 JURGENS, T.G., and TAFLOVE, A.: 'Three-dimensional contour FDTD modelling of scattering from single and multiple bodies', *IEEE Trans.*, 1993, **AP-41**, pp. 1703–1708
4 RAILTON, C.J., CRADDOCK, I.J., and SCHNEIDER, J.B.: 'Improved locally distorted CPFDTD algorithm with provable stability', *Electron. Lett.*, August 1995, **31**, (18)
5 RAILTON, C.J., and CRADDOCK, I.J.: 'A modified CPFDTD algorithm for the analysis of arbitrary 3D PEC structures', *IEE Proc. Microw. Antennas Propag.*, 1996, **143**, (5), pp. 367–372
6 HOLLAND, R.: 'Finite difference solutions of Maxwell's equations in generalized nonorthogonal coordinates', *IEEE Trans.*, 1983, **NS-30**, (6), pp. 4589–4591
7 FUSCO, M.: 'FDTD algorithm in curvilinear co-ordinates', *IEEE Trans.*, 1990, **AP-38**, pp. 76–89
8 LEE, J.F., PALANDECH, R., and MITTRA, R.: 'Modelling three-dimensional discontinuities in waveguides using non-orthogonal FDTD algorithm', *IEEE Trans.*, 1992, **MTT-40**, pp. 346–352
9 HARMS, P.H., LEE, J.F., and MITTRA, R.: 'A study of the nonorthogonal FDTD method versus the conventional FDTD technique for computing resonant frequencies of cylindrical cavities', *IEEE Trans.*, 1992, **MTT-40**, pp. 741–746
10 STRATTON, J.A.: 'Electromagnetic theory' (McGraw-Hill, New York, 1941), pp. 38–47
11 HOLLAND, R.: 'A finite difference time-domain EMP code in 3D spherical coordinates', *IEEE Trans.*, 1983, **NS-30**, (6), pp. 4592–4595
12 HAO, Y., and RAILTON, C.J.: 'Analysing electromagnetic structures with curved boundaries on cartesian FDTD meshes', (submitted for publication)
13 YU, C.-C., and CHU, T.-H.: 'Analysis of dielectric-loaded waveguide', *IEEE Trans.*, 1990, **MTT-38**, pp. 1333–1338
14 ROTHWELL, E.J., and FRASCH, L.L.: 'Propagation characteristics of dielectric-rod-loaded waveguide', *IEEE Trans.*, 1988, **MTT-36**, pp. 594–600
15 MARCUVITZ, N.: 'Waveguide handbook' (Peter Peregrinus London 1986)